

The role of ink-bottle pores in freeze-thaw damage of oolitic limestone

Maxim Deprez^{a,*}, Tim De Kock^{a,b}, Geert De Schutter^c, Veerle Cnudde^{a,d}

^aUGCT – PProGress, Dept. of Geology, Ghent University, Krijgslaan 281/S8, 9000 Ghent, Belgium

^bAntwerp Cultural Heritage Sciences (ARCHES), University of Antwerp, Blindestraat 9, 2000 Antwerp, Belgium

^cMagnel-Vandepitte Laboratory, Dept. of Structural Engineering and Building Materials, Ghent University, Technologiepark-Zwijnaarde 60, 9052 Gent, Belgium

^dDept. of Earth Sciences, Utrecht University, Princetonlaan 8a, 3584 CB Utrecht, The Netherlands

HIGHLIGHTS

- Freeze-thaw weathering of Savonnières limestone was investigated.
- Macroscopic behaviour was characterized by strain and temperature measurements.
- Microscopic observations of crystal and water localities were done with μ CT.
- The presence of oolitic ink-bottle pores decreases the frost susceptibility.

ARTICLE INFO

Article history:

Received 13 August 2019

Received in revised form 30 January 2020

Accepted 18 February 2020

Available online 25 February 2020

Keywords:

Freeze-thaw weathering

Critical saturation

Pore-scale

Strain

X-ray computed micro-tomography

ABSTRACT

Many natural building stones are altered when subjected to freeze-thaw (FT) cycles. On the one hand, the sensitivity of a material to FT damage has been quantified in the past by the existence of a material-specific critical water saturation. On the other hand, it was noticed that natural stones with a high volume of ink-bottle pores, normally hold a relatively large FT resistance. The relationship between the pore structure, the saturation and the FT resistance is however not well understood. In this paper, the influence of water content and the porosity on FT behaviour is investigated macroscopically with temperature and strain measurements, established techniques in FT related research, and X-ray computed micro-tomography (μ CT). Strain measurements performed on Savonnières limestone samples clearly show an increasing expansion with increasing water content, with the existence of a critical water saturation level between 70 and 80%. Differential X-ray imaging on differently saturated limestone samples in an unfrozen and frozen state then aided in explaining the origin of this critical saturation degree. By draining water from surrounding micro-pores through cryo-suction, ink-bottle ooid voids served as expansion reservoirs. When the majority of the ooid voids is water saturated prior to freezing, these voids lose their expansion reservoir ability and damaging pressures arise when water freezes inside undrained micro-pores. These findings not only help to understand the FT resistance of this limestone, but also give insight in the general FT behaviour of materials with bi- or multimodal pore-size distributions.

© 2020 Elsevier Ltd. All rights reserved.

1. Introduction

Freeze-thaw (FT) weathering is one of the main degradation processes for porous building materials, such as natural stones [1,2], cementitious materials [3] and bricks [4,5]. FT damage is the result of internal pressures caused by ice crystallization in the pores of the material, of which the magnitude depends on the pore structure and moisture content [6], and environmental drivers such as cooling rate, minimal temperature and time [7,8]. In the past, a material-specific critical water saturation degree

was noticed above which the porous medium immediately fails upon freezing [9–12]. When a subject had a moisture content below this threshold, weathering occurs over time in terms of fatigue failure [13].

To date, it is not fully understood how the water-ice phase transition generates damaging pressures. The founder of the critical saturation concept [14], attributes the damaging stresses to the 9% volume expansion coinciding with the water-ice phase transition [15] and hydraulic pressures [16]. The latter pressures are supposed to be generated by expulsion of water into small pores by the 9% volumetric expansion. Contradicting observations [17,18] however caused to doubt the hydraulic pressure theory and, nowadays, crystallization pressures [19–21] are mostly considered as

* Corresponding author.

E-mail address: Maxim.Deprez@UGent.be (M. Deprez).

the most damaging actors coinciding with crystallization in pores [22]. The crystallization pressure is founded on the chemical potential of water and ice [23]. As smaller crystals have a decreased melting point, the pore size r_p in which crystallization can occur is linked to the temperature T following:

$$T - T_m = \frac{2\gamma_{cl}}{(r_p - \delta)\Delta S_{fv}} \quad (1)$$

With T_m the melting temperature of large crystals (0 °C), γ_{cl} the specific energy of the ice-water interface (0.04 J/m²) and ΔS_{fv} the entropy of fusion per unit volume (1.2 J/cm³.K) and δ the thickness of a water film between the crystal and the pore wall [20]. Therefore, a negative temperature, or undercooling, is necessary to enable ice to percolate in smaller pores. The presence of a 0.9 nm thick water film between the ice crystal and pore wall [20] sustains disjoining pressures between both solid phases. These pressures are referred to as crystallization pressures. The pressure that is exerted by an ice crystal in a cylindrical pore can then be estimated by the capillary pressure of the crystal faces:

$$P_c = \frac{\gamma_{cl}}{r_p - \delta} \quad (2)$$

Which indicates that the crystallization pressure P_c is higher in smaller pores.

Many researchers have attempted to find correlations between the pore characteristics, moisture content and the occurrence of FT damage. A positive correlation was found between the critical saturation level of natural stones and their 'trapped' porosity [10,24,25]. These large micrometric to millimetric pores are separated from the macro-connected pore network by very small nanometric ones. Therefore, the trapped porosity is often referred to as 'ink-bottle' pores [26–28]. This phenomenon causes the ink-bottle pores to remain air-filled during imbibition. Ice nucleation within these pores causes a chemical potential gradient and, as a consequence, unfrozen water migrates towards the growing ice [23]. This water can crystallize then without confinement. Therefore, empty ink-bottle pores are considered to act as an expansion reservoir upon freezing [29]. Also in engineered cementitious materials, air voids are introduced into the matrix to increase the frost resistance [30,31]. It was noticed that air voids might serve as cryopumps and that high pressures arise when water freezes in capillary pores that are not connected to an air void [16,32].

Most of the statements concerning the crystallization process are however derived from indirect proxies, such as strain and temperature measurements [7,10,29,33]. Moreover, a large fraction of the previously mentioned researchers does not incorporate crystallization pressures as one of the main damaging mechanisms, but attribute the damage to hydraulic pressures. Therefore, direct proof is needed to better understand the FT related processes on the pore-scale. Only once the pore-scale processes are fully understood, large-scale FT weathering phenomena can be explained.

To investigate the influence of ink-bottle porosity and water saturation level on the micro- and macro-scale behaviour towards a FT cycle, the French Savonnières limestone was selected and several petrophysical parameters were characterised. This stone is widely used as building and replacement stone [34] and, additionally, it contains a vast amount of ink bottle porosity [35]. X-ray computed micro-tomography or micro-CT (μ CT [36]) data was gathered from two stone samples subjected to FT cycles to map the water redistribution and ice formation on the pore scale. This non-destructive technique enables to image different stages in the FT cycle consecutively on small samples [36]. Most importantly, the *in situ* observations were then linked to results of macro-scale strain experiments. This unique combination of

micro- and macro-scale observations has the ability to unravel the damaging mechanisms in porous limestone.

2. Materials

Savonnières limestone is a Jurassic (Tithonian) oolitic buff-coloured grainstone [37] from east of the Paris basin (Barrois, France) and is frequently used as building and replacement stone mainly in Western Europe [34,37,38]. Savonnières has a cross-bedded texture with encounters of bivalve-rich layers. The limestone is partially cemented with isopachous sparite and has a high secondary porosity [37] caused by partial or full dissolution of the ooids' core [39]. Both the partial cementation and the high amount of secondary porosity are reflected in the total porosity, which lies between 30 and 40 vol% [34,35,40]. The pores can be divided into four categories based on their location and size [35] (Figs. 1 and 2). In between the ooids, bounded by the sparite cement is the macroscopic inter-granular porosity (10–100 μ m). The pores between single sparite crystals are the microscopic inter-granular pores (0.1–1 μ m). Through secondary dissolution of the core of the ooids, many of them are vacuolar, leading to a large macroscopic intra-granular porosity (10 μ m–1 mm) in this text referred to as ooid voids. These macroscopic pores are connected to the inter-granular pores through microscopic channels (microscopic intra-granular pores; 1–100 nm). Altogether, this implies a multimodal pore-size distribution. The large porosity and partial cementation lead to relatively low strength properties. Derluyn (2012) [41] measured many mechanical properties of the limestone with a compressive and tensile strength of a wet sample perpendicular to the bedding plane of respectively 18.8 MPa and 1.46 MPa. Despite these relatively low strength values, the stone has a relatively high FT resistance.

3. Methods

3.1. Sample preparation and stone characterization

A total of six cylindrical samples of 20 mm diameter and 38 mm height were drilled for the strain and temperature measurements (S1–S8). To obtain high resolutions with the μ CT imaging technique, smaller cylindrical samples are necessary [36]. Therefore, two other cylindrical cores (8 mm diameter, 25 mm height) were prepared for μ CT experiments (S1ct & S2ct). The total porosity p_0 and bulk density ρ_b of all samples were measured using standardized hydrostatic weighing [42], for which the samples were saturated with distilled water at a 99 KPa vacuum. Additionally, three cylinders (S7, S8 and S1ct) were gradually immersed in distilled water for 48 h under atmospheric conditions. From this, the water absorption under atmospheric conditions could be compared to the absorption under vacuum. The same characterization tests were performed on a large building block (SB1; 150 × 90 × 50 mm) to compare the values obtained for the relatively small cylinders to overall values. On this block, several elastic parameters were determined using ultrasonic pulse velocity (Geotron Elektronik) and compared to parameters used by Derluyn (2012). These elastic properties are important to calculate stresses from the strain/temperature data.

3.2. Water saturation

The degree of water saturation (%) is defined as the fraction of pore volume that is filled with water. Consequently, the total pore volume, or effective porosity, of the sample needs to be known. From this, it is calculated how much water a dry sample needs to absorb or a wet sample needs to drain to obtain a certain

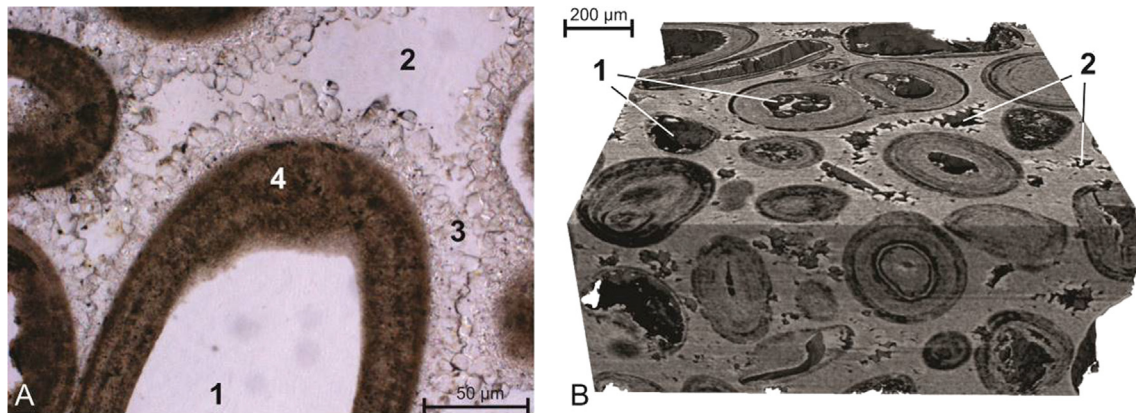


Fig. 1. A) microscopic image of a Savonnières limestone thin section with intra-granular macro-pores (1), inter-granular macro-pores (2), inter-granular micro-pores (3) and intra-granular micro-pores (4). B) 3D volume rendering of μ CT data of a Savonnières limestone with a voxel size of 1.3 μ m. The complex pore network is visible with the macroscopic intra-granular (1) and inter-granular pores (2). The micro-pores are not visible due to resolution restrictions.

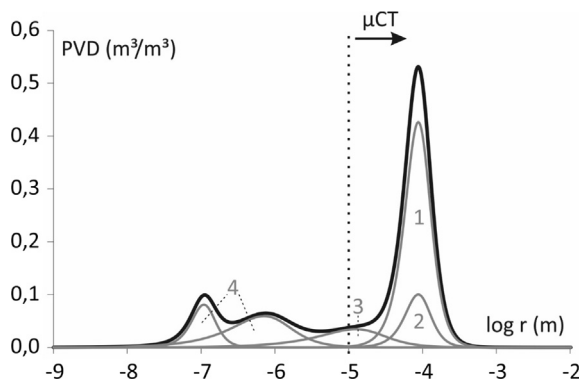


Fig. 2. The pore-size distribution of Savonnières derived by Roels et al. (2001) with the logarithm of the pore radius ($\log r$) plotted against the partial volume distribution (PVD) of the pores. The numbers in the graphs refer to the same pore-categories as in Fig. 1. The vertical dashed line gives in indication of the pores that are visible with the lab-based μ CT technique. These have typically a pore radius larger than 10 μ m (adapted from [35]).

saturation level, by measuring the respective weights. This amount of water can be reached in two ways: by drying of a fully saturated sample (saturation by drainage) or by imbibition of a dry sample (saturation by wetting) until the appropriate weight is reached. There is however often a hysteresis between the wetting and the drainage curve over time, which is defined by the pore network. Hence, different pores will be filled or drained depending on the saturation method. An explanation for the drainage and imbibition hysteresis of Savonnières limestone is given by Roels et al. (2001) [35]. This hysteresis points out that ovoid voids will be saturated last by wetting and will also drain last during drying of the stone. Locations of water prior to freezing are important to explain the results of the experiments and, therefore, both saturation methods will be used and compared in following experiments.

3.3. Temperature and strain measurements

In each of the eight cores (S1-S8), a hole of 1 mm diameter and 10 mm depth was drilled in the middle to insert a thermocouple later. First, samples were brought to a fixed water saturation degree by drying of the vacuum saturated samples until appropriate weight was reached (dry sample + water content at different degrees). To avoid evaporation or uptake of moisture during the experiments, the saturated cores were sealed with aluminium foil and wrapped in plastic tape. The aluminium foil serves to

distribute the temperature around the sample. The samples were left at 4 °C for 24 h to homogenise and equilibrate the water distribution within the pores. To prevent interference of extruding ice during the strain measurements, the top and bottom of the sample are stripped from their seal and dried partially. This was done by placing both sides on a dry cloth for 5 min and by blowing air over both surfaces for two minutes.

Subsequently, the samples were subjected to a FT cycle based on the European standard for determination of FT resistance of natural building stones [43] in a climatic test chamber (Weiss WKL 34/70). Due to the smaller size of the samples, it was decided to shorten the cycle from the standard 12 h to 6 h. Furthermore, the maximum temperature was kept at 10 °C to prevent additional moisture loss. The temperature was fixed at 10 °C for half an hour before it was decreased to -15 °C gradually during the next 1.5 h. Then the temperature remained fixed at -15 °C for another half an hour before it had 1.5 h to ascend to 10 °C again. Afterwards the temperature remained at 10 °C for another 2 h. A drawing of the climatological program can be found in Fig. 3B.

During the FT cycle, both the temperature and the length of the sample were monitored (Fig. 3A). For this purpose, two K-type thermocouples (Pico Technology SE028 and TC-08 data logger) were attached to each saturated core sample. The first thermocouple was inserted into the drilled hole to measure the inner temperature, while the second made contact with the upper flat surface of the stone cylinder. The saturated cores were then put into a custom-made invar holder on which LVDTs (Solartron Metrology Orbit3) were mounted on the top of the sample.

To investigate the behaviour in capillary saturated conditions, a first FT experiment was performed with samples S7 and S8 capillary saturated by wetting for 48 h (48%). A second FT experiment was conducted on samples S1 to S6, each having an increasing saturation degree obtained by drainage: 50, 60, 70, 80, 90, 100 % respectively.

3.4. μ CT experiments

Sample S1ct was capillary saturated and the pores contained 61% of water after 24 h. Sample S2ct was fully saturated with demineralized water by imbibition under vacuum and dried until the sample had 87% saturation. Both samples were wrapped in aluminium foil and plastic tape to prevent moisture loss, and acclimated in the 18 °C scanner bunker for an hour. Both samples were weighed both before and after the experiments to ensure a constant moisture level.

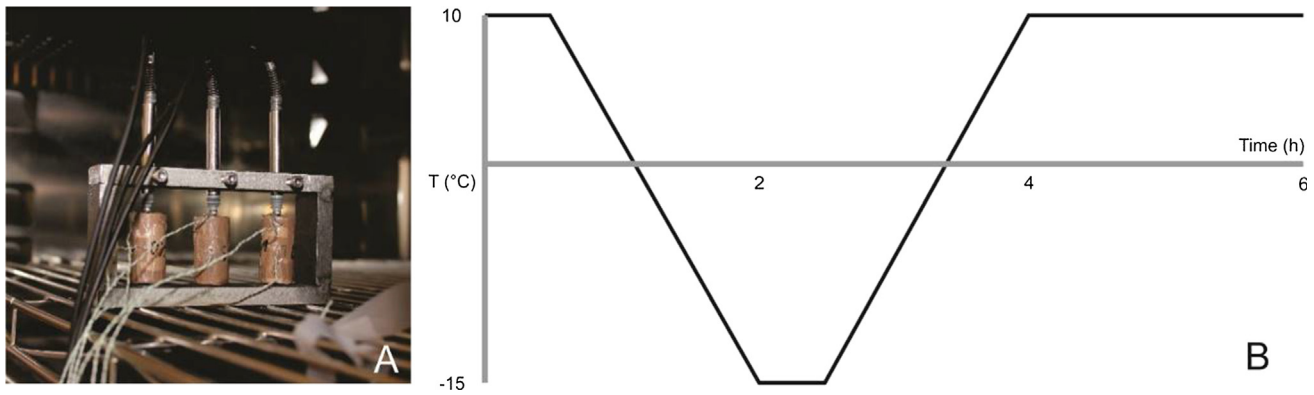


Fig. 3. A) The setup with the enwrapped stone samples under linear variable differential transducers (LVDTs), attached to a custom-made invar holder. Two thermocouples (white wires) were connected to each stone. B) A systematic drawing of the temperature program used for the experiments.

X-ray computed micro-tomography (μ CT) was performed at the Ghent University Centre for Tomography (UGCT) with the HECTOR setup (Fig. 4) [44,45]. HECTOR, short for High Energy CT Optimized for Research, consists of an XWT 240-SE microfocus source from X-RAY WorX, which can deliver a target power up to 280 W, and a PelkinElmer 1620 CN3 DX flat panel detector and a rotational stage capable of lifting objects up to 80 kg. For the experiments presented here, the tube was operated at a maximum high voltage of 190 kV and a maximum power output of 10 W. An aluminium slide of 0.5 mm thick was placed in front of the X-ray source to filter out the low-energy X-rays. Hence, beam hardening artefacts were largely eliminated from the dataset. A total of 2600 projections were taken with an acquisition time of 1 s. The resulting images had a reconstructed voxel size of 7 μ m. A feature within the μ CT images has to consist of multiple voxels to be distinguishable. This is the spatial resolution of the data and, for this research, it is set at three times the voxel size (21 μ m).

μ CT was performed before and after the samples were frozen. The samples were conditioned in a custom-made freezing cell [46], which was already deployed in similar experiments performed by De Kock et al. (2015). This device can cool cylindrical specimens with a maximal diameter of 1.4 cm and height of 3 cm down to -20 °C. The cooling device was controlled wirelessly by a LabView interface. A first μ CT scan was done when the

temperature was fixed at 10 °C, followed by another scan half an hour later when the sample was cooled and stable at -10 °C. Afterwards, the sample was heated to 10 °C and imaged again.

The raw μ CT data were reconstructed using Octopus Reconstruction [47] (Tescan XRE). Registration of the reconstructed images, segmentation and analysis was done in Avizo (ThermoFisher Scientific). The porosity of the sample was determined by segmenting all the pores, both air and water filled, and deriving the total 3D volume of those. Both water and ice were segmented at the same grey values and quantified in the same manner.

To compare the μ CT images before and after freezing, the differential imaging technique was used [48]. The unfrozen volume served as a reference of which a target volume, which is the frozen volume in this case, was subtracted. This way, the changes were highlighted that occurred between both acquisition moments. Areas where volume was added or removed compared to the reference then appeared white or black respectively. Areas wherein no change between the target and the reference volumes occurred remained grey. Both black and white areas were segmented from the subtracted dataset. To correct for slight offsets created in the image registration or slight movements of grains, a binary operation (opening) was performed on these segmented images. Afterwards, these images were analysed and visualised separately with 3D visualization software VGStudio 3.0 (Volume Graphics).

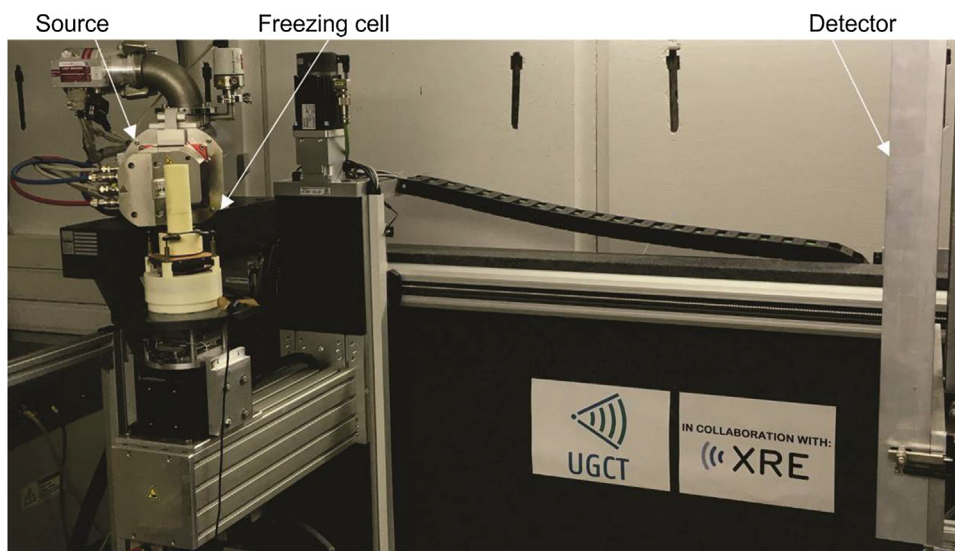


Fig. 4. The HECTOR setup with X-ray source on the left and flat panel detector on the right. The custom-made freezing stage is placed in front of the source.

4. Results & discussion

4.1. Material properties

The measured material properties are found in Table 1. The water content by total immersion under atmospheric pressure ($S_{L, atm}$) tends to vary between different samples. This is due to the heterogeneity within the Savonnières limestone. Additionally, the saturation levels ($S_{L, test}$) during the FT experiments are given for every sample. Since the top and bottom surfaces of cylinders S1-S8 are dried, maximally 3% of the water disappeared. Hence, the saturations are never exactly a multiple of ten.

Several elastic parameters were determined from ultrasonic sound velocity measurements on SB1. The bulk modulus of the porous medium (K_p) is 10.8 GPa. The elastic modulus (E) is 17.47 GPa which falls in the range of 14.7–20.4 GPa determined by [39,49]. Likewise, the Poisson’s coefficient (ν) of 0.25 fits with the observations of approximately 0.26 [49]. The bulk modulus of the solid (K_s) is estimated at 63.25 GPa, a value that was taken from measurements on a similar limestone [50]. A tensile strength value for Savonnières limestone of 1.46 MPa was found by [41].

4.2. Temperature and strain during FT cycles

An FT cycle was performed in a climate test chamber in which strain measurements were combined with temperature measurements to characterize the macroscopic behaviour of differently saturated Savonnières limestone samples (S1-S8). To be able to comment on the graphs (Figs. 5 and 7) properly, they are divided in zones along the time-axis, ranging from I to V.

4.2.1. Samples saturated by water immersion under atmospheric pressure (48%)

Temperature and strain of the S_{atm} samples (S7-S8) during a FT cycle are visualized in Fig. 5. At positive temperatures, the strain is proportional to the linear thermal expansion coefficient of the unfrozen stone (α_u). The cooling of the samples is interrupted by an exothermic peak after a period of undercooling (zone I). This exotherm is a proxy for ice crystallization within the sample and it coincides with a very small expansion, which is a thermal expansion as reaction to the sudden temperature rise to 0 °C.

In zone II, the temperature of the sample remains at the equilibrium melting temperature, 0 °C in this case. This temperature is defined by the pore size in which crystals are growing [19]. If crystallization would occur in micro-pores, the equilibrium temperature would be negative. Therefore, at this point, crystal growth continues in macroscopic pores and the temperature remains at the equilibrium 0 °C as long as enough latent heat is produced by the crystallization process. The period in which the temperature

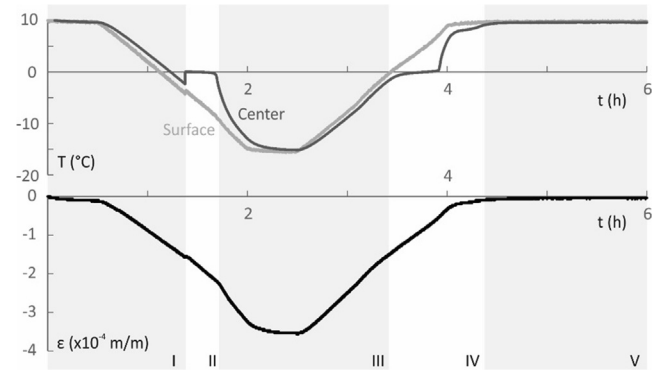


Fig. 5. The temperature (T) and strain (ϵ) evolution during a FT cycle of 48% saturated sample S8. Different events in the temperature inside (dark grey) and at the surface (light grey) and the strain (black line) facilitate the division of the T and ϵ evolution into five zones.

remains 0 °C is often referred to as the zero curtain [51–54]. Once most of the water in the macroscopic pores has crystallized, the produced latent heat cannot compensate the external cooling and the temperature of the limestone will decrease.

In zone III (Fig. 5), the strain is proportional to the thermal expansion coefficient of stone-ice composite (α_f). The thermal expansion coefficient of ice ($50 \times 10^{-6}/K$ [55]) is much larger than α_u ($5.8 \times 10^{-6}/K$). Consequently, α_f is higher than α_u . This is noticed by the steeper slope in the T- ϵ curve (Fig. 6). After thawing of the ice in zone IV, the behaviour of the sample is once more regulated by α_u (zone V). No residual strain is noticed, which was expected since the limestone is known to be FT resistant.

During the zero curtain in zone II (Fig. 5), the slope of the average T- ϵ curve is steeper than the slopes proportional to α_u and α_f (Fig. 6c). This contraction is most likely due to negative pressures that are created in the unfrozen pore water by ice crystallization [20].

The fact that the surface temperature and the inner temperature differ during crystallization and melting causes different T- ϵ curves, as displayed in Fig. 6. This raises the awareness of a temperature gradient within these samples. The temperature at the upper surface is more proportional to that of the climatic test chamber, while the temperature inside the sample is mostly regulated by the latent heat production. This should be taken into account to analyze these data and, therefore, the average temperature between the inner and surface temperature is also presented in Fig. 6c. The average temperature (T)-strain (ϵ) plot is more linear than the inner T- ϵ plot (Fig. 6a), while it takes into account the phase changes, which are barely visible in the surface T- ϵ plot (Fig. 6b). However, it should be remarked that since the

Table 1

Material properties of the tested samples with m_d the dry mass, p_0 and ρ_b the porosity and apparent density respectively determined by water absorption, $S_{L, atm}$ represents the saturation degree by total immersion obtained after 48 h imbibition. $S_{L, test}$ shows the saturation degrees of the stones when subjected to the FT cycles. The * represents tests with samples saturated by wetting.

Sample	Shape	m_d (g)	p_0 (%)	ρ_b (kg/m ³)	$S_{L, atm}$ (%)	$S_{L, test}$ (%)
SB1	prism	1176.66	33.64	1801	60	/
S1	cylinder	19.31	36.08	1751	/	48
S2	cylinder	19.24	35.10	1754	/	57
S3	cylinder	19.22	35.63	1743	/	67
S4	cylinder	19.6	34.92	1764	/	78
S5	cylinder	19.68	34.51	1778	/	88
S6	cylinder	19.68	34.00	1779	/	97
S7	cylinder	19.69	34.32	1769	48	48*
S8	cylinder	19.78	34.23	1777	48	48*
S1ct	cylinder	4.28	30.04	1892	61	61*
S2ct	cylinder	4.19	34.79	1765	65	87

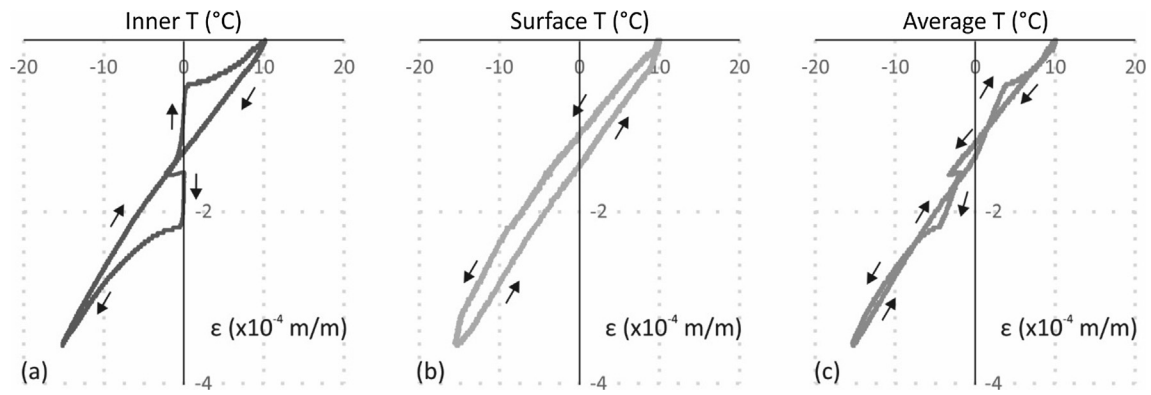


Fig. 6. Each graph comprises a plot of the strain observed in sample S8 against a specific sample temperature. In (a) the temperature in the centre is plotted, while (b) and (c) contain the surface temperature and the average between both temperatures respectively. The arrows indicate the time dimension as shown in Fig. 5.

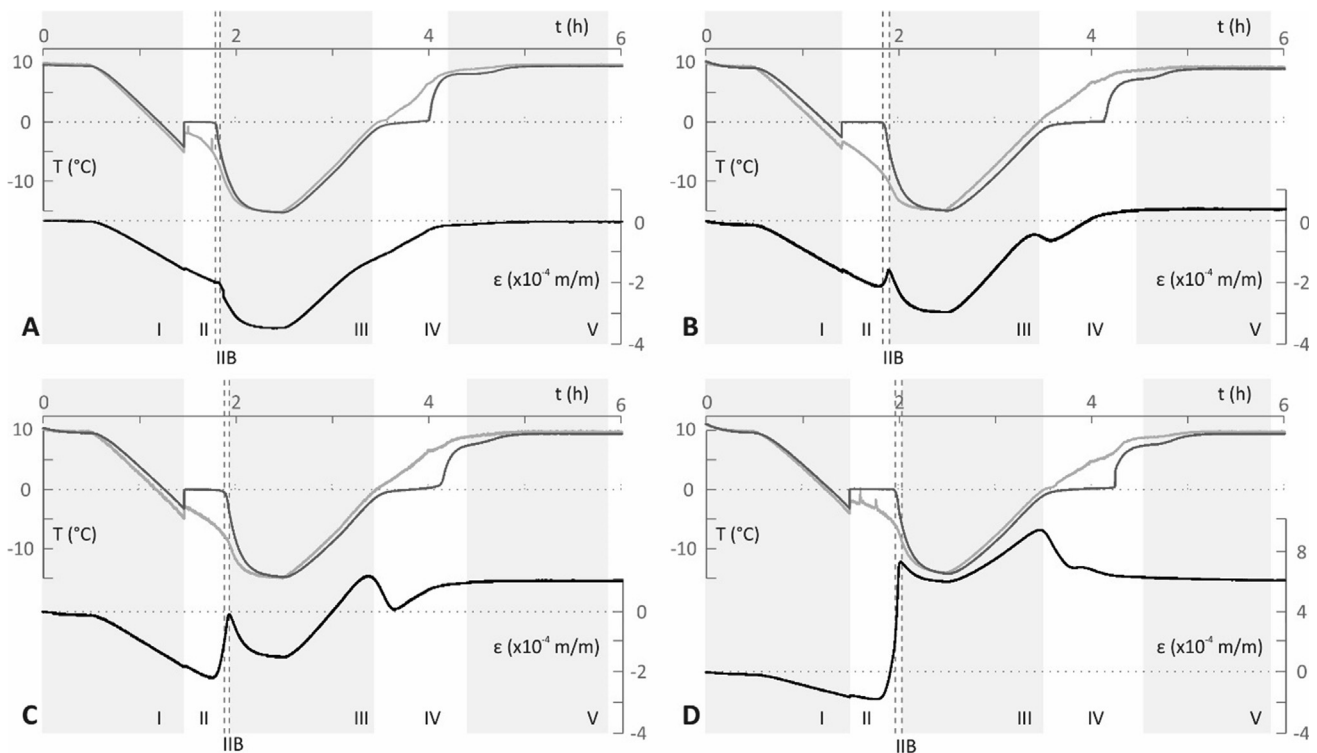


Fig. 7. The evolution of the inner temperature (dark grey), surface temperature (light grey) and strain (black) of the 70% (A), 80% (B), 90% (C) and 100% (D) water saturation during the first of three FT cycles. Different than in Fig. 4, an expansion that is increasing with degree of saturation is initiated near the end of zone II. This expansion continues until the end of zone IIB.

temperature is a moving front, an actual single sample temperature does not exist in this research and the average temperature is merely an approximation.

4.2.2. High water saturation (50–100%)

A FT cycle was performed on samples (S1–S6) with saturation levels starting from 50% while measuring temperature and strain (Fig. 7). The 50 and 60% saturated samples exhibit the same temperature-strain relation as the S_{atm} samples described in the previous section. This changes for saturations exceeding 70%, with an expansion appearing at the end of the crystallization phase (Fig. 7, zone IIB). The amplitude of this expansion phase becomes progressively larger in the subsequent 80, 90 and 100% saturated samples. A positive residual strain after thawing is observed for these samples. These observations imply that the critical saturation

degree is between 70 and 80% water saturation. With increasing water content, the residual strain increases exponentially.

After nucleation, a zero curtain is noticed, and ice therefore crystallizes in the macro-pores (zone II). The beginning of zone IIB is based on the temperature decrease in the centre of the sample, while its end is marked by the end of the expansion phase. During the zero curtain in zone II, the water that resides in the micropores remained in a liquid state. Now that the temperature decreases in zone IIB, crystallization will initiate in the micropores. These crystals will exert significant pressures on the pore walls and this will translate into expansion of the sample. The crystallization pressures are hence responsible for the strain in the samples.

The onset of expansion is however rooted in zone II (Fig. 7). This indicates the importance of a moving cold front in the samples. As the surface temperature is becoming progressively lower and the latent heat production decreases, a cold front will move from the

outside inwards. The water remaining inside the micro-pores will crystallize once this cold front passes its location. Hence, crystallization pressures are generated along this front and the total pressure budget will continue rising until it reaches the centre. This also means that the temperature in the centre at the end of the expansion, is the temperature related to the smallest pore radius in which water is freezing (Eq. (1)). For all cycles in which zone IIb is noticed, this temperature lies between -3.56 and -5.15 °C, with an average of -4 °C. Using Eqs. (1) and (2), the corresponding average pore radius is 17 nm and the crystallization pressure is 2.4 MPa. This calculated pore radius is slightly larger than the smallest pores (1 nm) present in the stone [35]. However, since the pore volume covered by pores smaller than 17 nm is less than 0.4% of the total pore volume and since no other expansive events are noticed, it is stated that crystallization of all the water is completed at this point.

The behaviour of the sample in zone III is again regulated by α_f . Near the end of zone III, however, the maximum strain is noticed in Fig. 7. This means that thawing is already occurring in this zone, before the temperature has reached 0 °C. Consequently, this is an indication of melting of crystals that are present in the micropores. Zone IV starts once the outer temperature has reached 0 °C and is characterized by melting of ice in macro-pores and the strain returns to either no strain, or to a residual strain.

From the T- ϵ curves in Fig. 8, several remarks can be made. First, the thermal expansion coefficients of the frozen samples (α_f) can be derived. The average α_u of all the samples was found at 5.8×10^{-6} . The α_f rises with increasing saturation degree from 10×10^{-6} at 50% saturated to almost 20×10^{-6} for the 100% saturated sample. Secondly, during the zero curtain, the average T- ϵ

curve again indicates a relatively high contraction of the sample, while the average temperature does not decrease much. This is usually attributed to negative pore pressures caused by the crystallization process. However, the large difference between surface and inner temperature and the presence of a progressing cold front during the zero curtain complicates attributing the strain during the zero curtain to a certain process. Third, when the temperature is raised again, it is important that the T- ϵ curves already decrease relative to α_f before the average sample temperature reaches 0 °C. This observation also indicates that thawing already occurs at temperatures lower than the melting point for macroscopic ice, and that ice has hence formed in the micro-pores during cooling.

4.3. μ CT imaging during FT cycles

To understand and verify the macroscopical behaviour, a microscopic study with μ CT was conducted. Two differently saturated drilled cores (Sct1 and Sct2) were subjected to three FT cycles while images were acquired when the sample temperature was stable at both 10 and -10 °C. These images were then used to calculate the water or ice content and to highlight water movement that occurred during the phase change. The porosity of the capillary saturated limestone sample (S1ct) was determined by placing the threshold for the pores at grey value 0 and 26,999 (16 bit), as shown in Fig. 9, and came to a total of 16.8% pore volume (P_{0CT}). This is approximately 55% of the porosity determined by hydrostatic weighing and, since the resolution of the μ CT images is 21 μ m, that means that 45% of the porosity has a smaller pore size. This observation fits with the model proposed by [35]. Moreover, the water content (S_{ICT}) was derived by segmenting grey values

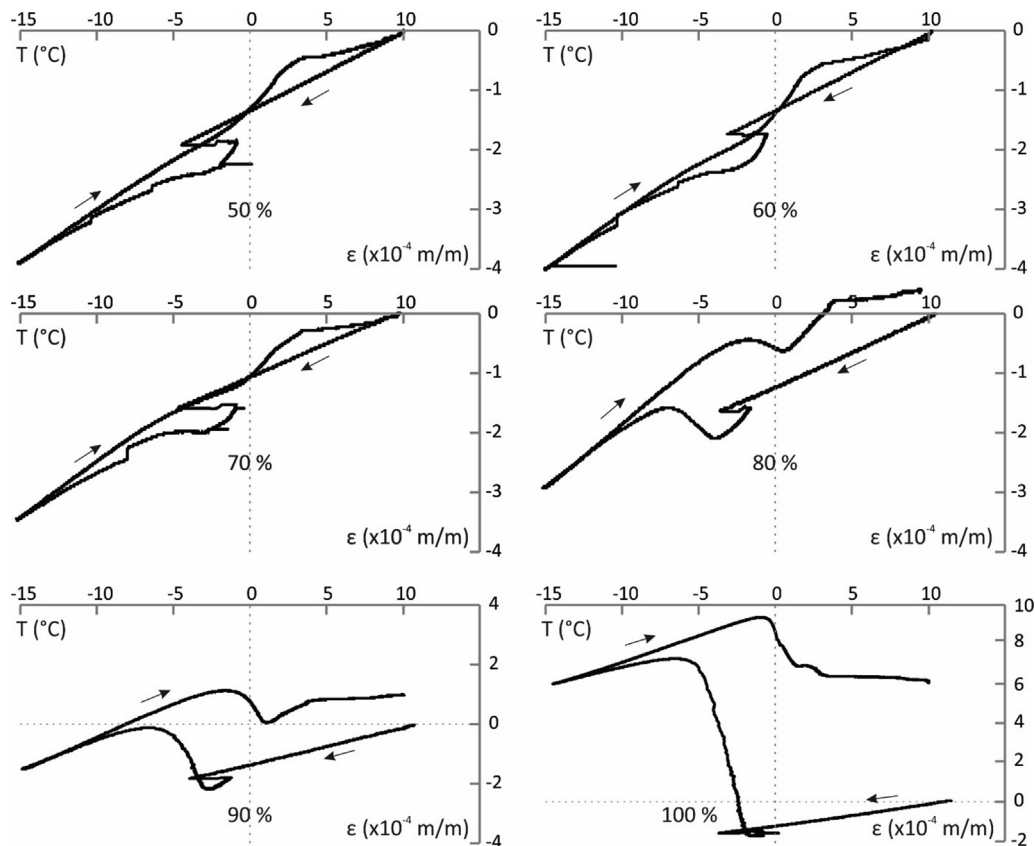


Fig. 8. Temperature-strain (T- ϵ) curves of the differently saturated samples. Residual strain is occurring from the 80% saturated sample onwards as the start and end positions of the curve do not coincide. The temperature is the average of the temperatures measured at the surface and the centre of the sample. The arrows indicate the evolution direction of the curves.

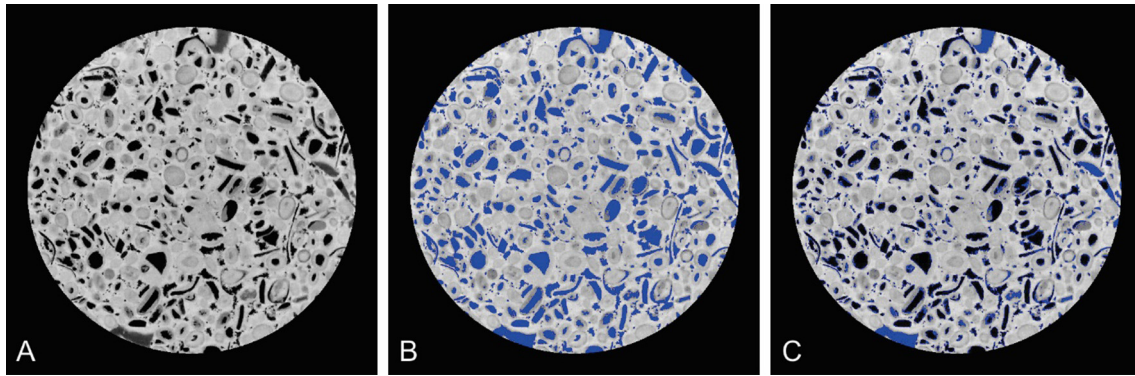


Fig. 9. After reconstructing the raw μ CT data of a cylindrical sample, a sequence of grey-value images as in A is created. Pores are almost black, while water or ice appears slightly paler. The stone matrix has the lightest grey value. The porosity can be calculated by segmenting all voxels with dark grey values linked to pores and water/ice (B, blue). In C, only the grey values of water/ice are segmented (in blue) and the water/ice content can subsequently be calculated. (For interpretation of the references to colour in this figure legend, the reader is referred to the web version of this article.)

18,000 to 26,999 and is 33.2% of that pore volume. The same grey values were segmented in the ice filled volume and the ice content was found to be 37.1%. The volume ratio of visible ice:water in frozen and unfrozen condition is 1.12. The volumetric expansion accompanying the phase change is set at 1.09. This implies that μ CT-unresolved water contributed to growth of the resolved, larger ice crystals. This water therefore originates from the smaller pores of the system.

The porosity (P_{0CT}) of the highly saturated sample (Sct2) was 19.9%, meaning that 57% of the porosity is visible with the obtained resolution of 21 μ m. This is in line with the previous sample and the pore-size distribution [35]. 78% of the visible porosity was filled with water prior to freezing and 86% with ice after freezing. The volumetric increase was therefore 1.09 and is equal to the volumetric expansion during the water-ice phase transition. Consequently, no additional water from the unresolved pores is used to build up the visible ice.

The porosity and water content values obtained by image analysis can be compared to the true values for these properties obtained by weighing saturated samples. The parameters obtained by both methods are listed in Table 2. By subtracting the porosity obtained by μ CT (P_{0CT}) from the effective total porosity (P_0), the total pore volume of pores smaller than the 21 μ m spatial resolution can be estimated (P_{micro}).

$$P_{micro} = P_0 - P_{0CT} \quad (3)$$

Furthermore, it is possible to calculate the water content in the μ CT-unresolved small pores by calculating the total volumes of water determined by both techniques, $P_0 \cdot S_L$ and $P_{0CT} \cdot S_{LCT}$, and subtracting the latter from the first. If the small pores of the system are completely filled with water, the following should be true.

$$\frac{(P_0 \cdot S_L) - (P_{0CT} \cdot S_{LCT})}{P_{micro}} \approx 1 (S_{Lmicro}) \quad (4)$$

This is the case for both of the sample as seen in Table 2. The micro-pores are therefore filled in both samples prior to freezing.

To visualize spatial differences between water and ice during unfrozen and frozen conditions, differential imaging [48] was applied on the μ CT datasets (Fig. 10). The differential images clearly show white areas, where mass appeared, and black areas,

where mass disappeared, within the sample (Fig. 10C). These areas can then be segmented and visualized separately (Fig. 10D). This technique was applied to μ CT data of the frozen and thawed samples. For visual purposes, the colours are changed in Fig. 11 from white and black to green and red respectively. The 60% saturated sample (Fig. 11A) is characterized by large red volumes in which water has disappeared upon freezing and many small evenly distributed green ice volumes. After thawing, most of the air-filled red volumes remain in place while green water volumes appear both in areas where ice was located during freezing and in pores that were air-filled both before and after cooling.

The 87% water-saturated sample Sct2 (Fig. 11B) displays the appearance of large ice volumes in green, while almost no water volume in red has disappeared after cooling to -10 $^{\circ}$ C. Moreover, many ice volumes were visible at the edge of the sample due to extrusion. These volumes are however not shown in Fig. 11B to visualize the inner water-ice movements. After thawing, the large ice volume has disappeared, however, many separate water volumes, in green, remain located in the position acquired during freezing. The pores that were drained upon freezing, remain air-filled (red) after thawing. Water has therefore not returned to those red pores.

The next step was to identify the specific pores that were preferentially drained or filled with ice. For this, the green and red volumes of Fig. 11 were compared to the pores in the original data. In 60% saturated Sct1, water was preferentially withdrawn from the inter-granular macro-pores, while ice then accumulated mostly in many small volumes at the inner rim of ooid voids (Fig. 12). For the highly saturated sample (Sct2), the ooid voids were fully water-filled prior to freezing, while a small part of the inter-granular macro-pores was air-filled. At -10 $^{\circ}$ C, these previously air-filled pores were filled with ice. Ice was hence extruded into these macro-pores and that process is also occurring at the sample surface. Hence, at high water saturations, ice will crystallize in the available accommodation space through extrusion.

4.4. The role of ink-bottle pores during FT cycling

The role of the different pores during the crystallization process can be derived by combining all the results gathered above.

Table 2
Values for porosity and water content determined by both hydrostatic weighing and μ CT.

Sample	P_0 (vol%)	S_L (vol%. P_0)	P_{0CT} (vol%)	S_{LCT} (vol%. P_0)	P_{micro} (vol%)	S_{Lmicro}
Sct1	30.0	61.4	16.8	33.2	13.2	0.97
Sct2	34.8	86.9	19.9	78.0	14.9	0.99

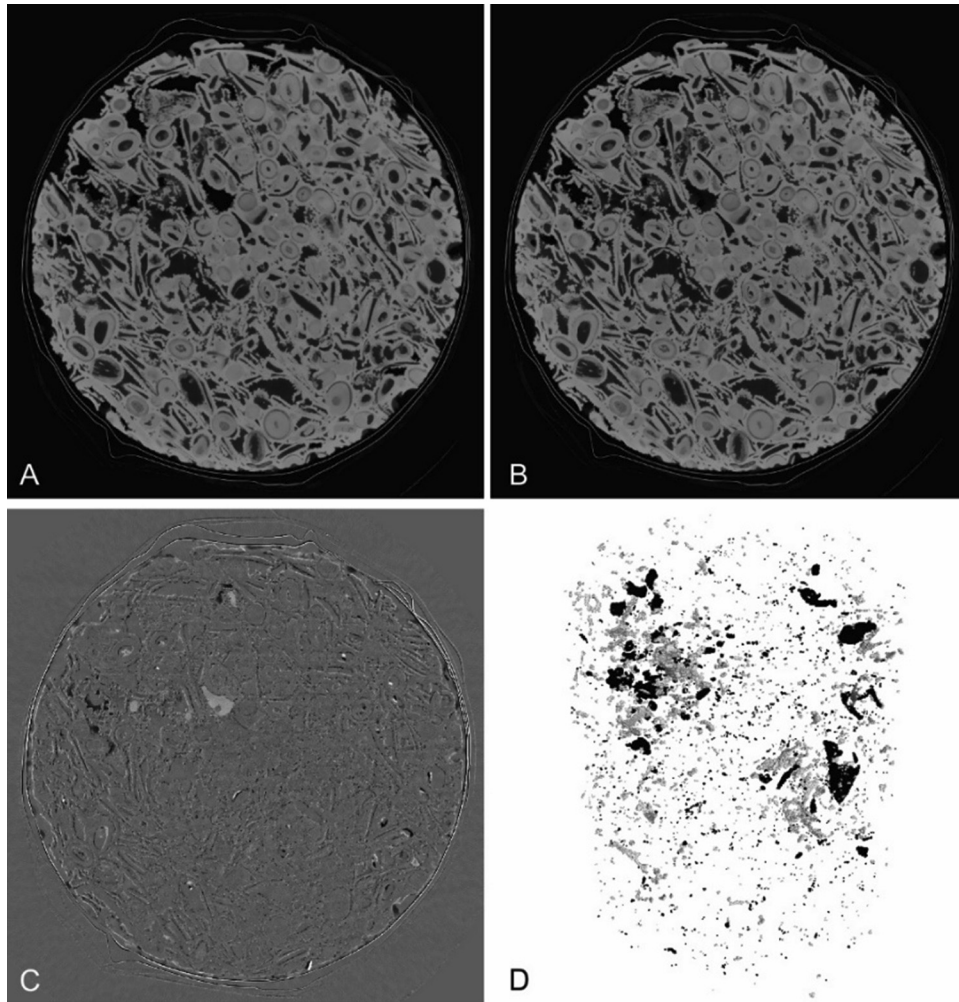


Fig. 10. A) xy-slice through a μ CT imaged limestone prior to freezing ($10\text{ }^{\circ}\text{C}$). B) The identical xy-slice after freezing ($-10\text{ }^{\circ}\text{C}$). C) Differential image as a result from subtracting image A from image B. D) Volume obtained by segmenting the white and black areas from a differential image sequence, with black where mass has disappeared and white where mass has appeared compared to the reference volume.

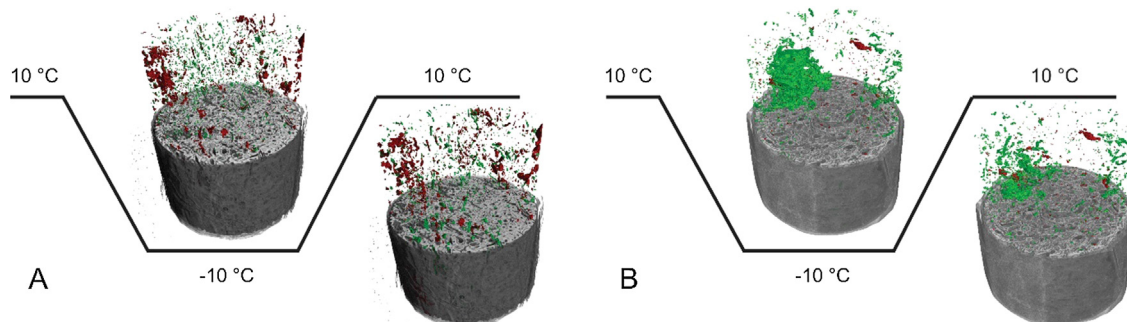


Fig. 11. 3D renderings of 60% (A) water-saturated sample in frozen ($-10\text{ }^{\circ}\text{C}$) and thawed ($10\text{ }^{\circ}\text{C}$) condition. The upper half of the sample is made invisible so that volumes of disappeared (red) and appeared mass (green) are clear. The 87% water-saturated sample is displayed in B. For generation of the coloured volumes, every μ CT scan was compared to a reference μ CT scan that was taken prior to freezing. (For interpretation of the references to colour in this figure legend, the reader is referred to the web version of this article.)

Despite of the limited coverage of the pore-size distribution by the μ CT images (Fig. 2), the observations combined with knowledge of total porosity confirm that most of the micro-pores are filled with water prior to freezing. The macro-pore filling depends on the saturation degree and method of saturation. If the stone was saturated using vacuum and subsequent drying, the ink-bottle ooid

voids will be filled prior to freezing. When the stone was saturated through wetting, the ooid voids will be empty.

Despite the micropores being filled with water at even low saturations, no strain is noticed during FT cycles. This is where the role of the ink-bottle ooid voids becomes clear. The μ CT data has shown that these voids become partially filled with ice around

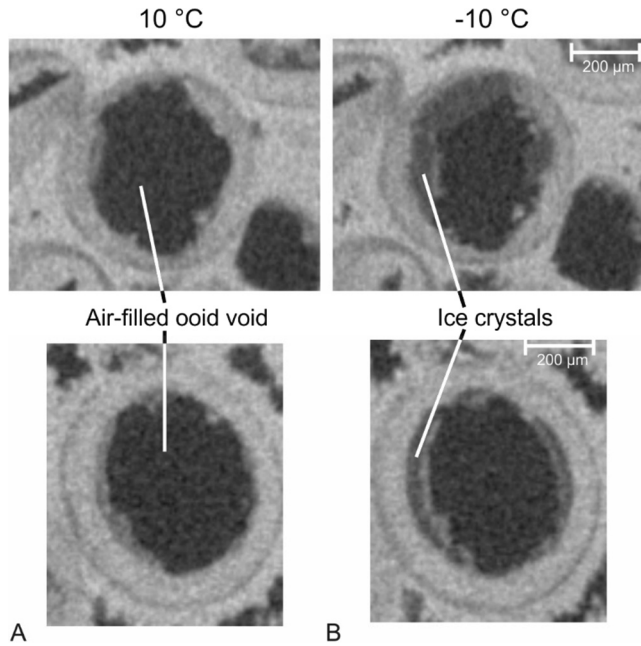


Fig. 12. A zoom on μ CT data of two selected ooid voids in the sample saturated by wetting. In unfrozen conditions (A), solely air is visible in the voids, while in frozen conditions (B), ice crystals have formed at the edge of the ooid void. This ice layer has an intermediate grey value, while the stone is light grey and the empty pore space is almost black.

the edges upon freezing (Fig. 12). Also, the volume of segmented ice is 12% more than the volume of segmented water in unfrozen conditions. This is 3% more than expected from the volume increase from the water-ice phase transition. This means that water that was at first invisible for the μ CT technique was used to build up the ice in the macro-pores. Altogether, this leads to the conclusion that the ooid voids are able to extract water from their neighbouring (micro-)pores. This process can be referred to as cryo-suction. Consequently, ice crystals can grow unconstrained within these ooid voids. This mitigates the risk for crystallization pressures in the micropores and subsequently the risk for damage. This is analogue to the processes occurring in cementitious materials [56], where the presence of large air voids increases the FT resistance. In cementitious materials, the nucleation occurs in the micro or meso-pores of the system at a certain level of undercooling [20,56]. This is supposed to cause hydraulic pressures in these small pores that forces water into the large air voids, in which the water crystallizes. These initial crystals in the air voids then provide the ability to drain the neighbouring micropores. Similarly, nucleation is observed in this research at undercooling temperatures ranging from -2 to -5 °C. This implies that nucleation most likely occurs in the micropores of this porous system and that the unfrozen pore water is hence forced into the ooid voids by hydraulic pressures.

When freezing highly saturated limestones, in which the ink-bottle ooid voids are mostly filled prior to freezing, the ooid voids can no longer drain the surrounding micropores. Instead, ice finds accommodation space by extruding into intergranular macro-pores. The volume of segmented ice from the μ CT images is exactly 1.09 of the segmented water volume. Therefore, the mass of macroscopically visible ice in frozen conditions equals the mass of macroscopically visible water in unfrozen conditions. This means that the mass of water/ice residing in the micro-pores remains the same before and after freezing. Consequently, a part of the water has to escape from the ooid voids to maintain the ice volume in the macro-pores. That water has to pass through connecting micro-pores to end up in the inter-granular

macro-pores where it eventually crystallizes. Since no positive strains are seen during the beginning of zone II (Fig. 7), no significant hydraulic pressures are generated through this process. This could be due to the open pore system, with many large pores connecting to smaller ones. Moreover, no broken ooids were seen after the three FT cycles, which also suggests merely limited stress caused by this transport.

4.5. Ice crystallization and FT damage

Temperature and strain measurements illustrate that once most of the water inside the macro-pores has crystallized, the temperature is able to decrease and water is able to freeze inside the micropores. This process generates crystallization pressures able to cause damage. With a higher saturation degree prior to freezing, more accommodation space inside the ooids will already be occupied. Hence, less water can be transported from the micro-pores towards the expansion reservoirs. An increasing saturation degree therefore causes more water to remain in the micro-pores and hence, more pore walls are prone to crystallization pressures when this water eventually crystallizes.

Under equilibrium conditions, crystallization pressures are however always offset by the negative pressure in the pore liquid. The latter can only be overcome by crystallization pressures during thermodynamical disequilibria, which can be caused in two ways. First, if the ice formation is very rapid, water is pushed towards the liquid-vapour menisci and as these are flattened, the pore pressure is no longer offsetting the crystallization pressure [20]. Consequently, the stone will expand until equilibrium is found. Secondly, once the temperature of the system starts to decrease, the large crystals formed in the macro-pores can additionally bulge into the micro-pores as the liquid-solid menisci start to decrease [19]. The interfacial energy however needs to be the same everywhere in the crystal and therefore, the crystal starts to melt at some points and water is transported by diffusion through the water film surrounding the crystal towards the pore entries of the micropores. This diffusion process is also very slow (10^{-12} – 10^{-13} m/s) compared to the cooling rate and, therefore, for large crystals, where the travel time is large, a disequilibrium is again maintained and transient stress arises in the crystal, causing crystallization pressures according to smallest crystal curvatures [57].

Earlier calculations have demonstrated that the crystallization pressures in a single pore with a radius of 17 nm is 2.4 MPa (Eq. (2)). This value already exceeds the tensile strength of the stone. However, to actually generate damage, a volume large enough to overcome the local tensile strength needs to be subjected to crystallization pressures [19]. Poromechanical theories allow us to calculate the total crystallization pressure over the entire volume ΔP_C [58]:

$$\Delta P_C = \frac{3K\varepsilon_f}{\beta_p S_C} \quad (5)$$

with K the bulk modulus (10.8 GPa), β_p the Biot coefficient (0.83), ε_f the linear strain and S_C the fraction of pores filled with ice. For fully frozen samples, it is assumed that for the maximal obtained strain ε_f , S_C is approximately 1.09 times the initial water saturation (S_L), to compensate for the 9% volume expansion. The total stress σ caused by crystallization pressures is then approximated by [59]:

$$\sigma \approx \beta_p S_C \Delta P_C \quad (6)$$

Poromechanics also allows calculation of the failure stress for Savonnières [58,59]:

$$\sigma > \frac{\sigma_t}{\sqrt{3(1-2\nu)}} \quad (7)$$

Table 3

The crystallization pressure over the entire volume (ΔP_c) is calculated by Eq. (5) for which residual strain and crystal content (S_c) is needed. The latter is 1.09 times the initial liquid content (S_L). The resulting stress (σ) is then calculated by Eq. (6).

S_L	S_c	residual strain	ΔP_c (MPa)	σ (MPa)
0.78	0.85	3.96E-05	1.82	1.28
0.88	0.95	1.02E-04	4.19	3.32
0.97	1.06	6.20E-04	22.82	20.10

With σ_t the tensile strength of the material (1.46 MPa [41]) and ν Poisson's ratio (0.25). Hence if the stress by crystallization pressure exceeds 1.19 MPa, theoretically, the stone will fail. ΔP_c can be estimated using the residual strain as ϵ_f in Eq. (5). The resulting stress over the volume (σ) can then be calculated by implementing ΔP_c in Eq. (6). For each sample that exhibited residual strain, the result of these calculations is found in Table 3. These poromechanical calculations show that the stress generated inside the 80% saturated sample slightly exceeds the 1.19 MPa threshold. This is a good match with the experimental temperature-strain data. Hence, the crystallization pressures over the entire volume are responsible for the observed residual strain.

When it comes to the critical saturation degree, it is clear the ooid voids are crucial. As long as these pores can serve as an expansion reservoir, immediate damage is not likely to occur. In capillary imbibition, the pore system of Savonnières limestone contains approximately 60% water without water-filled ooid voids. In this study, this saturation was never sufficient to cause (visible) damage. This explains the relatively good frost resistance of the Savonnières limestone, in spite of it being so porous. Under natural conditions, FT damage to Savonnières limestone is more likely to occur because of fatigue stresses, caused by repeated crystallization. Despite the unsubstantial nature of these pressures compared to the theoretical damage threshold, crystallization pressures can reach high values very locally, where it can overcome local tensile strength values.

5. Conclusion

In this paper, a combination of strain measurement and μ CT during FT cycles was used to clarify the mechanical reasons for the critical saturation degree of Savonnières limestone. While the μ CT technique proved its value in monitoring the (re-)distribution of water and ice through limestone samples, the temperature and strain monitoring gave insights in the pressure development upon freezing. This novel approach is therefore very valuable to assess the overall FT damage mechanisms of porous materials.

Ink-bottle pores, here in the form of ooid voids, are crucial for the FT resistance of natural stones. When atmospherically saturated, these pores remain dry prior to freezing. During crystallization, crystals formed within these pores are able to drain surrounding micro-pores. Therefore, the amount of water in the micro-pores of the system is reduced and this has a mitigating effect on the risk for elevated crystallization pressures within these small pores. In highly saturated samples, the accommodation space for ice inside the ooid voids is reduced. Therefore, these voids lose their ability to serve as expansion reservoirs. Water remains in the micro-pores where it can generate stresses able to overcome the tensile strength of the stone.

Residual strain is purely attributed to crystallization pressures generated in micropores. This is supported by thermodynamical and poromechanical calculations of the crystallization pressures within single pores and over the volume of entire samples. The stress generated by crystallization pressures at 80% saturation approximated the theoretical failure stress. Therefore, the critical saturation degree of this stone is between 70 and 80% water saturation. The limestone could only be atmospherically saturated up

to 60% of its pore volume, which clarifies the rather good frost durability of the stone.

CRedit authorship contribution statement

Maxim Deprez: Conceptualization, Investigation, Methodology, Formal analysis, Visualization, Writing - original draft. **Tim De Kock:** Conceptualization, Investigation, Supervision, Writing - review & editing. **Geert De Schutter:** Writing - review & editing, Supervision, Resources. **Veerle Cnudde:** Writing - review & editing, Supervision, Resources.

Declaration of Competing Interest

The authors declare that they have no known competing financial interests or personal relationships that could have appeared to influence the work reported in this paper.

Acknowledgments

This work was supported by Research Foundation – Flanders (FWO), project G.0041.15N. Tim De Kock was a postdoctoral fellow of the FWO and acknowledges its support. We are grateful to ROCAMAT to supply the natural stones used for the experiments and to Arnaud Frisque for help in the laboratory. The Ghent University Special Research Fund (BOF-UGent) is acknowledged for the financial support to the Centre of Expertise UGCT (BOF. EXP.2017.007). The authors would like to thank the two anonymous reviewers for their valuable comments.

Data availability

The data on the strain and temperature measurements is available in the Mendeley Data repository. The μ CT data will be made public on the 'Digital Rocks Portal' [60].

References

- [1] D.T. Nicholson, F.H. Nicholson, Physical deterioration of sedimentary rocks subjected to experimental freeze-thaw weathering, *Earth Surf. Process. Landforms* 25 (2000) 1295–1307, [https://doi.org/10.1002/1096-9837\(200011\)25:12<1295::AID-ESP138>3.0.CO;2-E](https://doi.org/10.1002/1096-9837(200011)25:12<1295::AID-ESP138>3.0.CO;2-E).
- [2] S. Noor-E-Khuda, F. Albermani, M. Veidt, Flexural strength of weathered granites: Influence of freeze and thaw cycles, *Constr. Build. Mater.* 156 (2017) 891–901, <https://doi.org/10.1016/j.conbuildmat.2017.09.049>.
- [3] M. Pigeon, J. Marchand, R. Pleau, Frost resistant concrete, *Constr. Build. Mater.* 10 (1996) 339–348, [https://doi.org/10.1016/0950-0618\(95\)00067-4](https://doi.org/10.1016/0950-0618(95)00067-4).
- [4] C. Thomachot, N. Matsuoka, M. Kuchitsu, M. Morii, Frost damage of bricks composing a railway tunnel monument in Central Japan: field monitoring and laboratory simulation, *Nat. Hazards Earth Syst. Sci.* 5 (2005) 465–476 (accessed May 28, 2018) <https://hal.archives-ouvertes.fr/hal-00299215/document>.
- [5] G. Wardeh, B. Perrin, Freezing-thawing phenomena in fired clay materials and consequences on their durability, *Constr. Build. Mater.* 22 (2008) 820–828, <https://doi.org/10.1016/j.conbuildmat.2007.01.004>.
- [6] Z. Rusin, P. Świercz, Frost resistance of rock materials, *Constr. Build. Mater.* 148 (2017) 704–714, <https://doi.org/10.1016/j.conbuildmat.2017.04.198>.
- [7] J. Ruedrich, S. Siegesmund, Salt and ice crystallisation in porous sandstones, *Environ. Geol.* 52 (2007) 225–249, <https://doi.org/10.1007/s00254-006-0585-6>.
- [8] J. Walder, B. Hallet, A theoretical model of the fracture of rock during freezing, *Geol. Soc. Am. Bull.* 96 (1985) 336–346 (accessed August 10, 2017).
- [9] G. Fagerlund, The significance of critical degrees of saturation at freezing of porous and brittle materials, in: *Conf. Durab. Concr. ACI STP*, New Jersey and Ottawa, Ontario, 1975, pp. 13–66, <https://doi.org/10.14359/17604>.
- [10] A. Prick, Critical degree of saturation as a threshold moisture level in frost weathering of limestones, *Permafrost. Process.* 8 (1997) 91–99, [https://doi.org/10.1002/\(SICI\)1099-1530\(199701\)8:1<91::AID-PPP238>3.0.CO;2-4](https://doi.org/10.1002/(SICI)1099-1530(199701)8:1<91::AID-PPP238>3.0.CO;2-4).
- [11] T.C.C. Chen, M.R.R. Yeung, N. Mori, Effect of water saturation on deterioration of welded tuff due to freeze-thaw action, *Cold Reg. Sci. Technol.* 38 (2004) 127–136 (accessed October 4, 2017) https://ac.els-cdn.com/S0165232X0300123X/1-s2.0-S0165232X0300123X-main.pdf?_tid=4189f04-a909-11e7-b032-00000a0b0f6c&acdnat=1507124742_21f1142f3792b8c514d87fd285e0e632.

- [12] A. Al-Omari, K. Beck, Á. Török, K. Beck, X. Brunetaud, M. Al-Mukhtar, Critical degree of saturation: a control factor of freeze-thaw damage of porous limestones at Castle of Chambord, France, *Eng. Geol.* 185 (2015) 71–80, <https://doi.org/10.1016/j.enggeo.2014.11.018>.
- [13] J. Martínez-Martínez, D. Benavente, M. Gomez-Heras, L. Marco-Castaño, M.Á. García-del-Cura, J. Martínez-Martínez, D. Benavente, M. Gomez-Heras, L. Marco-Castano, M.A. Garcia-Del-Cura, Non-linear decay of building stones during freeze-thaw weathering processes, *Constr. Build. Mater.* 38 (2013) 443–454, <https://doi.org/10.1016/j.conbuildmat.2012.07.059>.
- [14] G. Fagerlund, The international cooperative test of the critical degree of saturation method of assessing the freeze/thaw resistance of concrete, *Matériaux Constr.* 10 (1977) 231–253, <https://doi.org/10.1007/BF02478694>.
- [15] J. Hirschwald, Die Prüfung der natürlichen Bausteine auf ihre Wetterfeständigkeit, W. Ernst & Sohn, 1908. https://scholar.google.be/scholar?hl=en&as_sdt=0%2C5&q=hirschwald+1908+&btnG= (accessed September 25, 2017).
- [16] T.C. Powers, R.A. Helmuth, Theory of volume changes in hardened portland-cement paste during freezing, *Highw. Res. Board Proc.* 32 (1953).
- [17] J.J. Beaudoin, C. Macinnis, The mechanism of frost damage in hardened cement paste, *Cem. Concr. Res.* 4 (1974) 139–147 (accessed September 20, 2017) http://ac.els-cdn.com/0008884674901288/1-s2.0-0008884674901288-main.pdf?_tid=1f9ed764-9de8-11e7-b33c-00000a0b0f6b&acdnat=1505900774_49582ca90c6b42bd4fe24e1e71cd44.
- [18] G.G. Litvan, Adsorption systems at temperatures below the freezing point of the adsorptive, *Adv. Colloid Interface Sci.* 9 (1978) 253–302, [https://doi.org/10.1016/0001-8686\(78\)85001-5](https://doi.org/10.1016/0001-8686(78)85001-5).
- [19] G.W. Scherer, Crystallization in pores, *Cem. Concr. Res.* 29 (1999) 1347–1358, [https://doi.org/10.1016/S0008-8846\(99\)00002-2](https://doi.org/10.1016/S0008-8846(99)00002-2).
- [20] G.W. Scherer, J.J. Valenza, Mechanisms of Frost Damage, *Mater. Sci. Concr. VII* (2005) 209–246. http://www.jvalenza.com/Pub/Mech_Frost.pdf (accessed August 18, 2017).
- [21] M. Steiger, Crystal growth in porous materials—I: the crystallization pressure of large crystals, *J. Cryst. Growth.* 282 (2005) 455–469, <https://doi.org/10.1016/j.jcrysgro.2005.05.007>.
- [22] T. De Kock, M.A. Boone, T. De Schryver, J. Van Stappen, H. Derluyn, B. Masschaele, Geert D. Schutter, V. Cnudde, A pore-scale study of fracture dynamics in rock using X-ray micro-CT under ambient freeze–thaw cycling, *Environ. Sci. Technol.* 49 (2015) 2867–2874, <https://doi.org/10.1021/es505738d>.
- [23] D.H. Everett, The thermodynamics of frost damage to porous solids, *Trans. Faraday Soc.* 57 (1961) 1541, <https://doi.org/10.1039/tf9615701541>.
- [24] M. Bellanger, F. Homand, J.M. Remy, Water behaviour in limestones as a function of pores structure: application to frost resistance of some Lorraine limestones, *Eng. Geol.* 36 (1993) 99–108, [https://doi.org/10.1016/0013-7952\(93\)90022-5](https://doi.org/10.1016/0013-7952(93)90022-5).
- [25] J. Eslami, C. Walbert, A.-L. Beaucour, A. Bourges, A. Noumowe, Influence of physical and mechanical properties on the durability of limestone subjected to freeze-thaw cycles, *Constr. Build. Mater.* 162 (2018) 420–429, <https://doi.org/10.1016/j.conbuildmat.2017.12.031>.
- [26] S. Diamond, Mercury porosimetry: an inappropriate method for the measurement of pore size distributions in cement-based materials, *Cem. Concr. Res.* 30 (2000) 1517–1525, [https://doi.org/10.1016/S0008-8846\(00\)00370-7](https://doi.org/10.1016/S0008-8846(00)00370-7).
- [27] K. Morishige, N. Tateishi, Adsorption hysteresis in ink-bottle pore, *J. Chem. Phys.* 119 (2003) 2301–2306, <https://doi.org/10.1063/1.1585014>.
- [28] S. Siegesmund, R. Sneath, Stone in architecture: Properties, durability, 2011. DOI: 10.1007/978-3-642-14475-2.
- [29] A. Prick, Dilatometrical behaviour of porous calcareous rock samples subjected to freeze-thaw cycles, *CATENA* 25 (1995) 7–20, [https://doi.org/10.1016/0341-8162\(94\)00038-G](https://doi.org/10.1016/0341-8162(94)00038-G).
- [30] T.C. Powers, The air requirement of frost resistant concrete, *Highw. Res. Board Proc.* 29 (1949) 184–211.
- [31] G. Fagerlund, The required air content of concrete, University of Lund, Lund Institute of Technology, Division of Building Materials, 1995. https://scholar.google.be/scholar?hl=en&as_sdt=0%2C5&q=Fagerlund%2C+G.+%281995%29.+%27The+required+air+content+of+concrete.%27+Proc.%2C+Int.+Workshop+on+Mass-Energy+Transfer+and+Determination+of+Building+Components%2C+BRI-Japan+and+CSTB-France (accessed September 24, 2017).
- [32] M.T. Hasholt, Air void structure and frost resistance: a challenge to Powers' spacing factor, *Mater. Struct.* 47 (2014) 911–923, <https://doi.org/10.1617/s11527-013-0102-9>.
- [33] C. Thomachot, N. Matsuoka, Dilatation of building materials submitted to frost action, *Geol. Soc. London, Spec. Publ.* 271 (2007) 167–177, <https://doi.org/10.1144/GSL.SP.2007.271.01.17>.
- [34] G. Fronteau, C. Schneider-Thomachot, E. Chopin, V. Barbin, D. Mouze, A. Pascal, Black-crust growth and interaction with underlying limestone microfascies, *Geol. Soc. London, Spec. Publ.* (2010), <https://doi.org/10.1144/sp333.3>.
- [35] S. Roels, J. Elsen, J. Carmeliet, H. Hens, Characterisation of pore structure by combining mercury porosimetry and micrography, *Mater. Struct.* 34 (2001) 76–82, <https://doi.org/10.1007/BF02481555>.
- [36] V. Cnudde, M.N. Boone, High-resolution X-ray computed tomography in geosciences: a review of the current technology and applications, *Earth-Sci. Rev.* 123 (2013) 1–17, <https://doi.org/10.1016/j.earscirev.2013.04.003>.
- [37] T. De Kock, J. Dewanckele, M. Boone, G. De Schutter, P. Jacobs, V. Cnudde, Replacement stones for Lede stone in Belgian historical monuments, *Geol. Soc. London, Spec. Publ.* (2013), <https://doi.org/10.1144/sp391.9>.
- [38] B. Graue, S. Siegesmund, B. Middendorf, Quality assessment of replacement stones for the Cologne Cathedral: mineralogical and petrophysical requirements, *Environ. Earth Sci.* 63 (2011) 1799–1822, <https://doi.org/10.1007/s12665-011-1077-x>.
- [39] M. Lebedev, M.E.J. Wilson, V. Mikhaltsevitch, An experimental study of solid matrix weakening in water-saturated Savonni eres limestone, *Geophys. Prospect.* 62 (2014) 1253–1265, <https://doi.org/10.1111/1365-2478.12168>.
- [40] S. Roels, J. Carmeliet, H. Hens, J. Elsen, Microscopic analysis of imbibition processes in oolitic limestone, *Geophys. Res. Lett.* 27 (2000) 3533–3536, <https://doi.org/10.1029/1999GL008471>.
- [41] H. Derluyn, Salt, transport and crystallization in porous limestone: Neutron - X-ray imaging and poromechanical modeling, *ETH Zürich* (2012).
- [42] EN 1936, "Natural stone test methods. Determination of real density and apparent density, and of total and open porosity," 1999.
- [43] EN 12371, "Natural stone test methods. Determination of frost resistance," 2008.
- [44] B. Masschaele, M. Dierick, D. Van Loo, M.N. Boone, L. Brabant, E. Pauwels, V. Cnudde, L. Van Hoorebeke, HECTOR: A 240kV micro-CT setup optimized for research, *J. Phys. Conf. Ser.* 463 (2013) 12012, <https://doi.org/10.1088/1742-6596/463/1/012012>.
- [45] M. Dierick, D. Van Loo, B. Masschaele, M.N. Boone, E. Pauwels, L. Brabant, V. Cnudde, L. Van Hoorebeke, Hector, a new multifunctional micro-CT scanner at UGCT, *EEE 10th Int. Symp. Biomed. Imaging From Nano to Macro*, 2013.
- [46] T. De Schryver, M.A. Boone, T. De Kock, B. Duquenne, M. Christaki, B. Masschaele, M. Dierick, M.N. Boone, L. Van Hoorebeke, A compact low cost cooling stage for lab based x-ray micro-CT setups, *AIP Conf. Proc.* (2014) 1–5, <https://doi.org/10.1063/1.4937512>.
- [47] J. Vlassenbroeck, M. Dierick, B. Masschaele, V. Cnudde, L. Van Hoorebeke, P. Jacobs, Software tools for quantification of X-ray microtomography at the UGCT, *Nucl. Instruments Methods Phys. Res. Sect. A Accel. Spectrometers, Detect. Assoc. Equip.* 580 (2007) 442–445, <https://doi.org/10.1016/j.nima.2007.05.073>.
- [48] M.A. Boone, T. De Kock, T. Bultreys, G. De Schutter, P. Vontobel, L. Van Hoorebeke, V. Cnudde, 3D mapping of water in oolitic limestone at atmospheric and vacuum saturation using X-ray micro-CT differential imaging, *Mater. Charact.* 97 (2014) 150–160, <https://doi.org/10.1016/j.matchar.2014.09.010>.
- [49] C. Walbert, J. Eslami, A.-L. Beaucour, A. Bourges, A. Noumowe, Evolution of the mechanical behaviour of limestone subjected to freeze-thaw cycles, *Environ. Earth Sci.* 74 (2015) 6339–6351, <https://doi.org/10.1007/s12665-015-4658-2>.
- [50] M. Lion, F. Skoczylas, B. Ledésert, Determination of the main hydraulic and poro-elastic properties of a limestone from Bourgogne, France, *Int. J. Rock Mech. Min. Sci.* 41 (2004) 915–925, <https://doi.org/10.1016/j.ijrmm.2004.02.005>.
- [51] D. Guilbert, S. Caluwaerts, K. Calle, N. Van Den Bossche, V. Cnudde, T. De Kock, Impact of the urban heat island on freeze-thaw risk of natural stone in the built environment, a case study in Ghent, Belgium, *Sci. Total Environ.* 677 (2019) 9–18, <https://doi.org/10.1016/j.scitotenv.2019.04.344>.
- [52] K. Hall, Evidence for freeze-thaw events and their implications for rock weathering in northern Canada, *Earth Surf. Process. Landforms* 29 (2004) 43–57, <https://doi.org/10.1002/esp.1012>.
- [53] K. Hall, Evidence for freeze-thaw events and their implications for rock weathering in northern Canada: II. The temperature at which water freezes in rock, *Earth Surf. Process. Landforms* 32 (2007) 249–259, <https://doi.org/10.1002/esp.1389>.
- [54] C. Hauck, Frozen ground monitoring using DC resistivity tomography, *Geophys. Res. Lett.* 29 (2002) 2016, <https://doi.org/10.1029/2002GL014995>.
- [55] T.R. Butkovich, Linear thermal expansion of ice, *US Army Snow Ice Permaf. Res. Estab. Corps Eng.* (1957).
- [56] Z. Sun, G.W. Scherer, Effect of air voids on salt scaling and internal freezing, *Cem. Concr. Res.* 40 (2010) 260–270, <https://doi.org/10.1016/j.cemconres.2009.09.027>.
- [57] G.W. Scherer, Internal stress and cracking in stone and masonry, in: *Meas. Monit. Model. Concr. Prop.*, Springer Netherlands, Dordrecht, 2006, pp. 633–641, https://doi.org/10.1007/978-1-4020-5104-3_77.
- [58] O. Coussy, Deformation and stress from in-pore drying-induced crystallization of salt, *J. Mech. Phys. Solids* 54 (2006) 1517–1547, <https://doi.org/10.1016/j.jmps.2006.03.002>.
- [59] R.M. Espinosa-Marzal, A. Hamilton, M. McNall, K. Whitaker, G.W. Scherer, The chemomechanics of crystallization during rewetting of limestone impregnated with sodium sulfate, *J. Mater. Res.* 26 (2011) 1472–1481, <https://doi.org/10.1557/jmr.2011.137>.
- [60] M. Prodanovic, M. Esteva, M. Hanlon, G. Nanda, P. Agarwal, Digital Rocks Portal: a repository for porous media images, (2015). DOI: 10.17612/P7CC7K.